Leonardo Marin, Andres Tarrasó, Ignacio Candela, Pedro Rodríguez. (2018) Stability analysis of a droop-controlled grid-connected VSC. ECCE 2018: IEEE Energy Conversion Congress and Exposition: Portland, OR, USA: Sept. 23-27, 2018: IEEE, 2018. Pp. 4161-4167 Doi: 10.1109/ECCE.2018.8558126.

Leonardo Marin, Andres Tarrasó, Ignacio Candela, Pedro Rodríguez. (2018) Stability analysis of a droop-controlled grid-connected VSC. ECCE 2018: IEEE Energy Conversion Congress and Exposition: Portland, OR, USA: Sept. 23-27, 2018: IEEE, 2018. Pp. 4161-4167 Doi: 10.1109/ECCE.2018.8558126.

Stability Analysis of a Droop-Controlled Grid-Connected VSC

Leonardo Marin, Andres Tarrasó, Ignacio Candela
Department of Electrical Engineering
Technical University of Catalonia
GAIA Building, Terrassa, Barcelona, Spain 08222
Email: leonardo.marin@upc.edu

Pedro Rodriguez
Universidad de Loyola
Sevilla, SPAIN
Email: prodriguez@uloyola.es

***Abstract*—In this paper a small signal stability analysis of a reverse droop-controlled grid-connected voltage source converter has been performed. The analysis includes the getting of a state-space representation of the system and the calculation of their participation factors.**

Special emphasis has been given to the influence of parameters such as the short circuit ratio, the bandwidth of the phase-locked and the constants of the droop controllers on the stability of the system.

***Index Terms*—small signal stability, droop control, state-space, eigenvalues, participation factors.**

I. Introduction

In the last decades, environmental considerations have lead to an important increase in the use of renewable energies such as wind and solar and this trend is expected to continue in the future [1]. However, integration of this type of energies into electrical systems is usually only possible by means of a suitable power electronics interface, such as Voltage Source Converters (VSC), that enables variables such as voltage and frequency to be controlled.

In the near future a large part of traditional generation based on conventional synchronous machines (SM) will be replaced by renewable generation based on voltage source converters (VSC). In such conditions a major problem will be the decrease of inertia –with its stabilizing effects– in relation to the total power of the system [2].

Therefore, research efforts have been directed at the design of power controllers that emulate the behavior of synchronous generators [3]. A first step in this direction is taken by droop controllers whose main objective is to participate in the grid voltage and frequency regulation or load sharing, in the same way as synchronous generators do through their droop characteristics, i.e., modifying the active and reactive power they inject proportionally to the frequency and voltage deviations [4].

There are two types of droop controllers: conventional droop control or simply droop control and reverse droop control [5]. In the first approach VSCs are controlled as voltage sources and they can operate in both grid-connected and island mode. On the other hand, in the reverse droop control VSCs are controlled as current sources and they can only operate in grid-connected mode.

Conventional droop control has been extensively studied [6–8]. Nevertheless, although most of distributed generation (DG) power converters are controlled as current sources, few researches have been found to analyse the reverse droop control strategy [5, 9, 10], and these are not focused on the stability of this control approach.

The paper derives a detailed non-linear state space model for the reverse droop control implementation, and a corresponding small signal model in order to apply linear analysis techniques to the system in the perspective of stability assessment. The effect of system parameters on the poles of the linearized system model is also analysed by calculating the participation factors of the system eigenvalues.

The rest of the paper is organized as follows: section II gives a brief description of the system under study. In section III a mathematical model of each of the components of the system is obtained. Based on the mathematical formulation of section III, a non-linear state-space model of the system is obtained in section IV. In order to apply classical stability assessment techniques based on eigenvalues, the system is linearized and a small-signal model is obtained in section V. Participation factor analysis and several graphs are obtained in VI. Finally, Section VII summarized the main conclusions of the work.

II. Control system overview

The system under consideration is a reverse-droop-controlled three-phase VSC connected to the grid through a LCL-filter. A simplified one-line diagram of the systems is shown in Fig. 1. For simplicity, the DC-link voltage v_{dc} has been assumed constant. Only balanced three-phase conditions have been assumed, i.e., voltages and currents contain only positive sequences. Boldface letters are used in this work to denote complex space vectors. Vectors and transfer functions referred to the stationary $\alpha\beta$-frame are denoted with the superscript s, whereas their counterparts in dq-frame are represented without this superscript. The switching dynamics of the VSC has been disregarded and an ideal average model is assumed for modelling the converter. The current control has been implemented in the dq-frame.

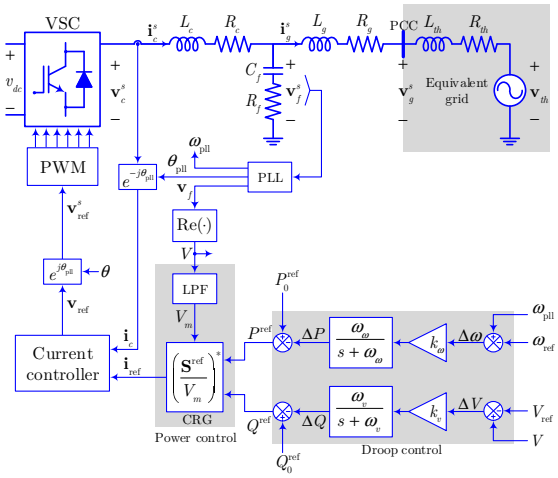

Fig. 1: One-line diagram of a droop controlled three-phase grid-connected VSC.

The overall AC grid that includes generators, transmission lines, loads, etc., has been replaced by its Thévenin equivalent, i.e., a voltage source in series with an equivalent impedance. This simple structure is assumed to achieve a non-complex model that includes the main dynamics of the converter control system and its interaction with the grid.

III. Mathematical model of the system

In this section, the process followed to obtain the state-space representation of the system described in the previous section is detailed. The system is composed by linear and non-linear sub-systems.

A. Phase locked loop (PLL)

Fig. 2 depicts the block diagram of the SRF-PLL, where the Park transformation is used for phase detection, and the output q-axis voltage is regulated by a PI controller, $G_c^{\text{pll}}(s)$, for phase tracking [11].

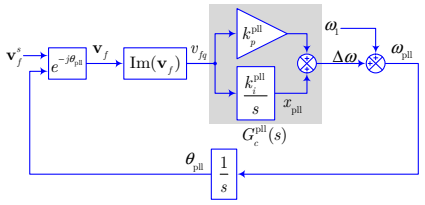

Fig. 2: Block diagram of the SRF-PLL.

From Fig. 2 one of the possible state space representations of the SFR-PLL is given by

$$\begin{aligned}\frac{d\theta_{\text{pll}}}{dt} &= k_p^{\text{pll}}\,\text{Im}\left(\mathbf{v}_f\right) + x_{\text{pll}} + \omega_1 \\ \frac{dx_{\text{pll}}}{dt} &= k_i^{\text{pll}}\,\text{Im}\left(\mathbf{v}_f\right)\end{aligned} \tag{1}$$

where the transformation of the synchronization voltage from $\alpha\beta$ to dq-frame through the Park transformation is given by (2) being θ_{pll} the phase detected by the PLL.

$$\mathbf{v}_f = \mathbf{v}_f^s e^{-j\theta_{\text{pll}}} \tag{2}$$

B. Droop control

As shown in Fig. 1, in the $P-\omega$ droop controller, the angular frequency ω_{pll} detected PLL, is compared with the rated or desired frequency ω_{ref}. The resulting frequency error is then amplified by the factor k_ω, low-pass filtered and finally subtracted from the desired active power generation P_0^{ref} to give as output, the final active power reference P^{ref}.

Similarly, the error signal $V - V_{\text{ref}}$ is the input of the $Q-V$ droop controller, and after of being amplified by a factor k_v, low-pass filtered and subtracted from the desired reactive power reference Q_0^{ref}, gives as output Q^{ref}.

From above, the final power references are given by

$$\begin{aligned}P^{\text{ref}} &= P_0^{\text{ref}} - \Delta P \\ Q^{\text{ref}} &= Q_0^{\text{ref}} - \Delta Q\end{aligned} \tag{3}$$

where

$$\begin{aligned}\Delta P &= k_\omega \frac{\omega_\omega}{s+\omega_\omega}\left(\omega_{\text{pll}} - \omega_{\text{ref}}\right) \\ \Delta Q &= k_v \frac{\omega_v}{s+\omega_v}\left(V - V_{\text{ref}}\right)\end{aligned} \tag{4}$$

Eq. (4) can be expressed in the time domain in the following way

$$\begin{aligned}\frac{d\Delta P}{dt} &= -\omega_\omega \Delta P - k_\omega \omega_\omega \left(\omega_{\text{pll}} - \omega_{\text{ref}}\right) \\ \frac{d\Delta Q}{dt} &= -\omega_v \Delta Q - k_v \omega_v \left(V - V_{\text{ref}}\right)\end{aligned} \tag{5}$$

The value of ω_{pll} can be obtained from (1), i.e.,

$$\omega_{\text{pll}} = \frac{d\theta_{\text{pll}}}{dt} = k_p^{\text{pll}}\,\text{Im}\left(\mathbf{v}_f\right) + x_{\text{pll}} + \omega_1 \tag{6}$$

On the other hand, in the steady state, the q component of $\mathbf{v}_f$ equals zero and the d component equals the voltage magnitude V, i.e.,

$$V = \text{Re}\left(\mathbf{v}_f\right) = v_{fd}, \qquad v_{fq} = 0 \tag{7}$$

C. Power control

Power regulation can be attained mainly through open and closed loop controls [12]. In this work, only the second approach has been considered. In this case, a direct conversion of reference powers to reference currents is performed, given the voltage at the synchronization point.

If 7 is satisfied, active and reactive currents could be directly calculated P^{ref}/V and $-Q^{\text{ref}}/V$ respectively. However, as it can be seen in Fig. 1, a low-pass filter (LPF) is included to filter the voltage magnitude V, given the low-pass filtered voltage V_m. If this LPF is not included, the current references might contain harmonic and noise, which in turn will result in the system instability by exciting LCL-filter resonance. Because of the relatively

low cut-off frequency required of this filter it can make an important contribution to the dynamics of the system and should be included in the model.

The low-pass filtered voltage and the voltage magnitude are related by means of

$$V_m = \frac{\omega_m}{s+\omega_m} V \tag{8}$$

where ω_m is the cut-off frequency of the LPF. Eq. (8) can be expressed in the time domain by means of

$$\frac{dV_m}{dt} = -\omega_m V_m + \omega_m V \tag{9}$$

The desired current references are calculated, using notation in complex numbers, by means of

$$\mathbf{i}_{\text{ref}} = i_d^{\text{ref}} + j i_q^{\text{ref}} = \left(\frac{\mathbf{S}^{\text{ref}}}{V_m}\right)^* = \frac{P^{\text{ref}}}{V_m} - j\frac{Q^{\text{ref}}}{V_m} \tag{10}$$

where $\mathbf{S} = P + jQ$ and the superscript $*$ denotes the complex conjugate.

D. Current control

1) Current controller: The current controller consists of a PI controller, $G_c(s)$, together with the inductor current feed-forward through the gain $j\omega L$, generally used when the current control is carried out in dq-frame to decouple the axes cross-coupling [13]. For simplicity, the PCC-voltage feed-forward [14] is not included.

The voltage reference $\mathbf{v}_{\text{ref}}$ is given by the following control law

$$\mathbf{v}_{\text{ref}} = G_c(s)\left(\mathbf{i}_{\text{ref}} - \mathbf{i}_c\right) + j\omega L \mathbf{i}_c \qquad G_c(s) = k_p + \frac{k_i}{s} \tag{11}$$

where $L = L_c + L_g$ and k_p and k_i are the proportional and integral gains of the PI current controller respectively. The controlled current is sensed in $\alpha\beta$ and the transformed to dq by using the PLL phase θ_{pll}, i.e.,

$$\mathbf{i}_c = \mathbf{i}_c^s e^{-j\theta_{\text{pll}}} \tag{12}$$

Equation (11) can be expressed in the time domain as follow

$$\begin{aligned} \frac{d\mathbf{x}_c}{dt} &= k_i\left(\mathbf{i}_{\text{ref}} - \mathbf{i}_c\right) \\ \mathbf{v}_{\text{ref}} &= k_p\left(\mathbf{i}_{\text{ref}} - \mathbf{i}_c\right) + \mathbf{x}_c + j\omega L \mathbf{i}_c \end{aligned} \tag{13}$$

where $\mathbf{x}_c = x_{cd} + j x_{cq}$. The variables x_{cd} and x_{cq} are two auxiliary states associated to the current controller but without any particular physical meaning.

The PI current controller acts on the current error and generates the voltage reference $\mathbf{v}_{\text{ref}}$ in dq. This voltage reference is then transformed to $\alpha\beta$ by

$$\mathbf{v}_{\text{ref}}^s = \mathbf{v}_{\text{ref}} e^{j\theta_{\text{pll}}} \tag{14}$$

2) Current control time delay: In the digital implementation of a current control for a two-level VSC with switching frequency f_{sw} and sampling frequency f_s, there is a time delay T_d incurred from computation and pulse width modulation (PWM) [15]. For the case of synchronous current sampling, either with single update ($f_s = f_{sw}$) or double update ($f_s = 2f_{sw}$), it is common to assume that the total time delay is given by [14]

$$T_d = 1.5T_s, \qquad T_s = \frac{1}{T_s} \tag{15}$$

of which T_s and $0.5T_s$ are due to computation and PWM, respectively. Due to the time delay, the voltage reference and the output voltage $\mathbf{v}_c^s$ of the VSC are related in $\alpha\beta$-frame by means of

$$\mathbf{v}_c^s = e^{-T_d s}\mathbf{v}_{\text{ref}}^s \tag{16}$$

If a first order Padé approximation is used in order to rationalize the factor $e^{-T_d s}$, (16) becomes

$$\mathbf{v}_c^s = \frac{2 - T_d s}{2 + T_d s}\mathbf{v}_{\text{ref}}^s \tag{17}$$

that can be expressed in the time domain as

$$\begin{aligned} \frac{d\mathbf{x}_d^s}{dt} &= -\frac{2}{T_d}\mathbf{x}_d^s + 4\mathbf{v}_{\text{ref}}^s \\ \mathbf{v}_c^s &= \frac{1}{T_d}\mathbf{x}_d^s - \mathbf{v}_{\text{ref}}^s \end{aligned} \tag{18}$$

where $\mathbf{x}_d = x_{d\alpha} + j x_{d\beta}$, and $x_{d\alpha}$ and $x_{d\beta}$ are two new auxiliary states.

3) LCL filter: From Fig. 1, the differential equations that define the dynamics of LCL-filter in the $\alpha\beta$-frame can be defined by means of Kirchhoff's voltage and current laws as

$$\begin{aligned} \frac{d\mathbf{i}_c^s}{dt} &= \frac{1}{L_c}\left(\mathbf{v}_c^s - \mathbf{v}_f^s\right) - \frac{R_c}{L_c}\mathbf{i}_c^s \\ \frac{d\mathbf{i}_g^s}{dt} &= \frac{1}{L_g}\left(\mathbf{v}_f^s - \mathbf{v}_g^s\right) - \frac{R_g}{L_g}\mathbf{i}_g^s \\ \frac{d\mathbf{v}_f^s}{dt} &= \frac{1}{C_f}\mathbf{i}_f^s + R_f\frac{d\mathbf{i}_f^s}{dt} \end{aligned} \tag{19}$$

E. Equivalent grid

The strength of the grid with regard to the VSC can be quantified by means of the short circuit ratio (SCR) [16] which is given by

$$\text{SCR} = \frac{1}{Z_{th}} \tag{20}$$

where Z_{th} is the per unit value of the equivalent impedance, where the base values are defined from the apparent power rating and the rated peak value of the phase voltage of the VSC. On the other hand, the inductive or resistive character of the equivalent grid is given by the quotient

$$q = \frac{L_{th}}{R_{th}} \tag{21}$$

To simulate the behavior of the system against different SCRs and different values of q, L_{th} and R_{th} can be calculated from

$$L_{th} = \frac{q}{\mathrm{SCR}\sqrt{1+q^2}}, \qquad R_{th} = \frac{1}{\mathrm{SCR}\sqrt{1+q^2}} \tag{22}$$

The injection of current into the grid through modifies the PCC voltage, which is given by

$$\mathbf{v}_g^s = \mathbf{v}_{th}^s + L_{th}\frac{d\mathbf{i}_g^s}{dt} + R_{th}\mathbf{i}_g \tag{23}$$

IV. Non-linear state space model of the system

All equations needed for detailed modelling of the system have been presented in the previous section, and can be reduced to a model on state-space form with 15 distinct state variables and 6 input signals, with the state vector $\mathbf{x}$ and the input vector $\mathbf{u}$ defined by (24) and (25) respectively. The resulting non-linear state-space model of the overall system is given by (26):

$$\begin{aligned}\mathbf{x} = \Big[&\theta_{\mathrm{pll}} \quad x_{\mathrm{pll}} \quad P \quad Q \quad x_{cd} \quad x_{cq} \quad x_{d\alpha} \quad x_{d\beta} \\ &i_{c\alpha} \quad i_{c\beta} \quad i_{g\alpha} \quad i_{g\beta} \quad v_{f\alpha} \quad v_{f\beta} \quad V_m\Big]^T\end{aligned} \tag{24}$$

$$\mathbf{u} = \Big[\omega_{\mathrm{ref}} \quad V_{\mathrm{ref}} \quad P_0^{\mathrm{ref}} \quad Q_0^{\mathrm{ref}} \quad \Delta v_{th\alpha} \quad v_{th\beta}\Big]^T \tag{25}$$

$$\begin{aligned}
\frac{d\theta_{\mathrm{pll}}}{dt} &= k_p^{\mathrm{pll}}\,\mathrm{Im}\left(\mathbf{v}_f\right) + x_{\mathrm{pll}} + \omega_1 \\
\frac{dx_{\mathrm{pll}}}{dt} &= k_i^{\mathrm{pll}}\,\mathrm{Im}\left(\mathbf{v}_f\right) \\
\frac{d\Delta P}{dt} &= -\omega_\omega \Delta P - k_\omega \omega_\omega \left(\omega_{\mathrm{pll}} - \omega_{\mathrm{ref}}\right) \\
\frac{d\Delta Q}{dt} &= -\omega_v \Delta Q - k_v \omega_v \left(V - V_{\mathrm{ref}}\right) \\
\frac{d\mathbf{x}_c}{dt} &= k_i\left(\mathbf{i}_{\mathrm{ref}} - \mathbf{i}_c\right) \\
\frac{d\mathbf{x}_d^s}{dt} &= -\frac{2}{T_d}\mathbf{x}_d^s + 4\mathbf{v}_{\mathrm{ref}}^s \\
\frac{d\mathbf{i}_c^s}{dt} &= \frac{1}{L_c}\left(\mathbf{v}_c^s - \mathbf{v}_f^s\right) - \frac{R_c}{L_c}\mathbf{i}_c^s \\
\frac{d\mathbf{i}_g^s}{dt} &= \frac{1}{L_g}\left(\mathbf{v}_f^s - \mathbf{v}_g^s\right) - \frac{R_g}{L_g}\mathbf{i}_g^s \\
\frac{d\mathbf{v}_f^s}{dt} &= \frac{1}{C_f}\mathbf{i}_f^s + R_f\frac{d\mathbf{i}_f^s}{dt} \\
\frac{dV_m}{dt} &= -\omega_m V_m + \omega_m V
\end{aligned} \tag{26}$$

V. Small-signal model of the system

State-space model in (26) is non-linear and classical stability assessment techniques based on eigenvalues are not directly applicable. So, in this subsection all the subsystems of previous section has been linearized at a specific operating point. The corresponding linearized small-signal state-space model can be expressed in the classical form

$$\Delta\dot{\mathbf{x}} = \mathbf{A}\Delta\mathbf{x} + \mathbf{B}\Delta\mathbf{u} \tag{27}$$

where the prefix Δ denotes small-signal deviations around the steady-state operating point.

Prior to the linearisation, the differential equations of the time delay and the LCL-filter that in (26) are expressed in $\alpha\beta$-frame, have been transformed to dq-frame. The state vector $\Delta\mathbf{x}$ and the input vector $\Delta\mathbf{u}$ defined by (28) and (29) respectively

$$\begin{aligned}\Delta\mathbf{x} = \Big[&\Delta\theta_{\mathrm{pll}} \quad \Delta x_{\mathrm{pll}} \quad \Delta P \quad \Delta Q \quad \Delta x_{cd} \ldots \\ &\ldots \Delta x_{cq} \quad \Delta x_{dd} \quad \Delta x_{dq} \quad \Delta i_{cd} \quad \Delta i_{cq} \ldots \\ &\ldots \Delta i_{gd} \quad \Delta i_{gq} \quad \Delta v_{fd} \quad \Delta v_{fq} \quad \Delta V_m\Big]^T\end{aligned} \tag{28}$$

$$\begin{aligned}\Delta\mathbf{u} = \Big[&\Delta\omega_{\mathrm{ref}} \quad \Delta V_{\mathrm{ref}} \quad \Delta P_0^{\mathrm{ref}} \ldots \\ &\ldots \Delta Q_0^{\mathrm{ref}} \quad \Delta v_{thd} \quad \Delta v_{thq}\Big]^T\end{aligned} \tag{29}$$

For reasons of space, matrices $\mathbf{A}$ and $\mathbf{B}$ are not included in this work.

VI. Participation factor analysis

If $\mathbf{\Psi}_i$ and $\mathbf{\Phi}_i$ are the left and right eigenvalues associated to the eigenvalue λ_i, a matrix called the *participation matrix*, $\mathbf{P}$, combines the right and left eigenvectors as follows [17]:

$$\mathbf{P} = \Big[\mathbf{p}_1 \quad \mathbf{p}_2 \quad \ldots \quad \mathbf{p}_n\Big] \tag{30}$$

with

$$\mathbf{p}_i = \begin{bmatrix}\psi_{i1}\phi_{1i} \\ \psi_{i2}\phi_{2i} \\ \vdots \\ \psi_{in}\phi_{ni}\end{bmatrix} \tag{31}$$

where ψ_{ik} and ϕ_{ki} are the kth entries of $\mathbf{\Psi}_i$ and $\mathbf{\Phi}_i$ respectively. Coefficients $p_{ki} = \psi_{ik}\phi_{ki}$ measure the correlation between the modes and the state variables and are referred as the *participation factors*. It is a measure of the relative participation of the kth state variable in the ith mode, and vice versa [17].

In this section, the participation factors analysis is carried out in order to clearly determine the relationship between the different states and the different eigenvalues of the system. The main parameters of the system are shown in Table I.

Fig. 3 shows the participation factors of the system, calculated for the operation point defined by the base case parameters shown in Table II. The values have been normalized in such a way that the largest of them has a value of 100 and values less than 1 have been neglected.

Although the system is stable for the parameters of Table I and operating conditions of Table II, it should be noted that the stability can be sensitive to variations in the system parameters.

TABLE I: Main circuit parameters

Electrical constant	Symbol	Value
Grid voltage (line-to-line)	V_{th}	400 V
Grid frequency	f_1	50 Hz
VSC Rated power	S_n	125 kVA
VSC DC-link voltage	v_{dc}	750 V
VSC switching frequency	f_{sw}	3.15 kHz
VSC sampling frequency	f_s	6.30 kHz
LCL-filter	L_c	777.6 µH
	R_c	7.3 mΩ
	L_g	402.2 µH
	R_g	2.1 mΩ
	C_f	66 µF
	R_f	500 mΩ

TABLE II: Base case parameters

Parameter	Value	Parameter	Value
k_ω	25 pu	$f_{\text{bw}}^{\text{pll}}$	20 Hz
k_v	20 pu	k_p^{pll}	86
f_ω [1]	20 Hz	k_i^{pll}	3728
f_v [2]	5 Hz	k_p	1
P_0^{ref}	0.6 pu	k_i	444
Q_0^{ref}	0.2 pu	T_d	0.24 ms
f_m [3]	100 Hz	SCR	5
		q	100

[1] $\omega_\omega = 2\pi f_\omega$ [2] $\omega_v = 2\pi f_v$ [3] $\omega_m = 2\pi f_m$

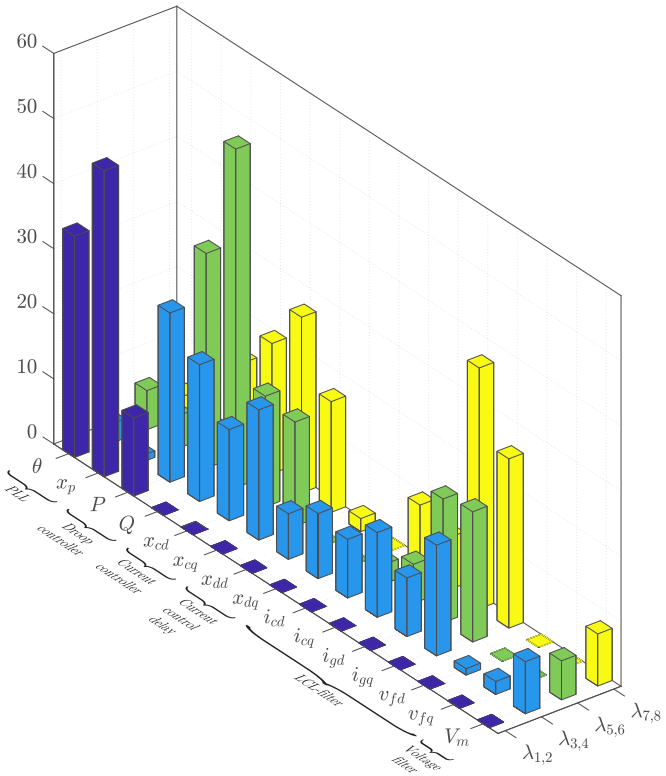

Fig. 3: Participation factors for the base case parameters.

There are several parameters that can cause instability in the system under certain conditions. Figs. 4 to 9 show the trajectory of the poles closest to the imaginary axis for the variation of SCR, $f_{\text{bw}}^{\text{pll}}$, k_ω, k_v, f_ω and f_v. The change of the pole location is indicated with a colour gradient, starting from blue and changing towards red. Points highlighted with black crosses are the eigenvalues for the base case parameters. It can be seen from the figures that eigenvalues move to the imaginary axis and cause the system instability when the indicated parameter reaches certain value.

Since the obtained system is of 15th order, it has 15 eigenvalues. Nevertheless only eigenvalues from $\lambda_{1,2}$ to $\lambda_{7,8}$ are considered the dominant eigenvalues and are shown in Figs. 3 to 9. This eigenvalues appear in 4 conjugate complex pairs. Eigenvalues from λ_{11} to λ_{16} are on the left half-plane, too far from the imaginary axis and therefore they have been neglected.

The joint observation of the participation factors and the eigenvalues trajectory shows that eigenvalues $\lambda_{1,2}$ are strongly related with the parameters of the PLL and $P-\omega$ droop controller. The remaining parameters have virtually no influence on these eigenvalues.

Eigenvalues $\lambda_{3,4}$, $\lambda_{5,6}$ and $\lambda_{7,8}$ are influenced to a greater or lesser extent with practically all the parameters of the system. However, it is important to note that in all cases, eigenvalues $\lambda_{3,4}$ determine the system stability since its real part becomes positive when the aforementioned parameters vary in the indicated manner.

Figs. 8 and 9 show that low pass filters of the $P-\omega$ and $Q-V$ droops are vital to make the system stable. The cut-off frequencies of these filters, $f_\omega = 55$ Hz and $f_v = 11$ Hz are relatively low. Without these filters, which is equivalent to infinite cut-off frequency, the system will be automatically unstable.

VII. Conclusions

In this paper small signal stability analysis of a reverse droop-controlled grid-connected VSC has been performed. In this sense, firstly a state-space model of the systems has been obtained. Then, participation factors analysis has been then performed for determining the influence of some relevant parameters in the root locus of system eigenvalues.

It is possible to conclude that the stability of the system decreases as the short circuit ratio is reduced. Similarly, it is possible to conclude that the relative stability of the system is reduced by increasing the PLL bandwidth or the coefficients of the droops of active and reactive power. In all cases, it is always the same eigenvalue that is most prone to instability.

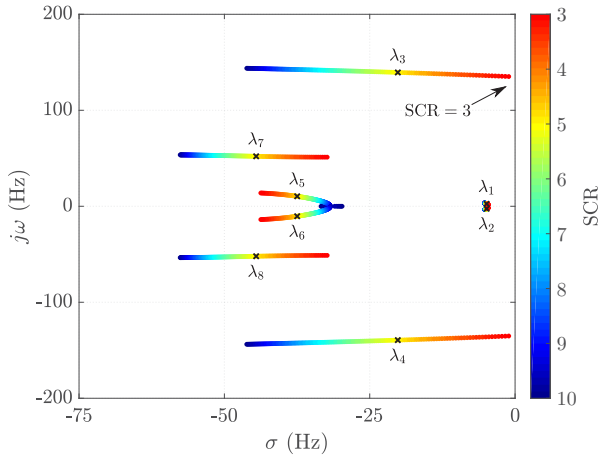

Fig. 4: Eigenvalue trajectory for a sweep of SCR from 10 to 3.

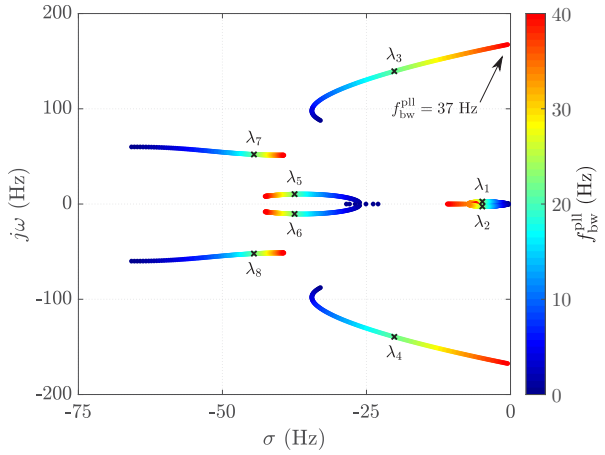

Fig. 5: Eigenvalue trajectory for a sweep of $f_{\text{bw}}^{\text{pll}}$ from 1 Hz to 37 Hz.

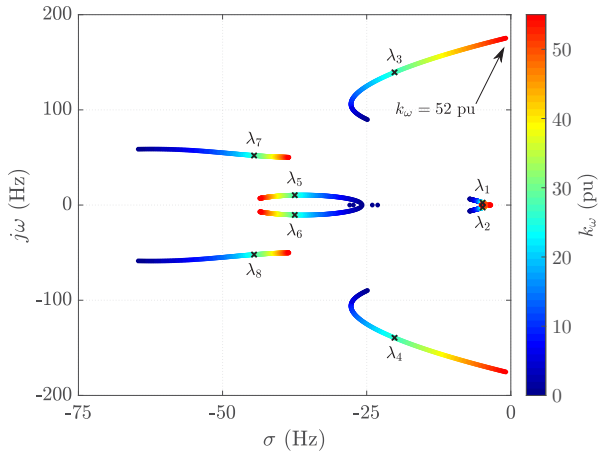

Fig. 6: Eigenvalue trajectory for a sweep of k_ω from 1 pu to 52 pu.

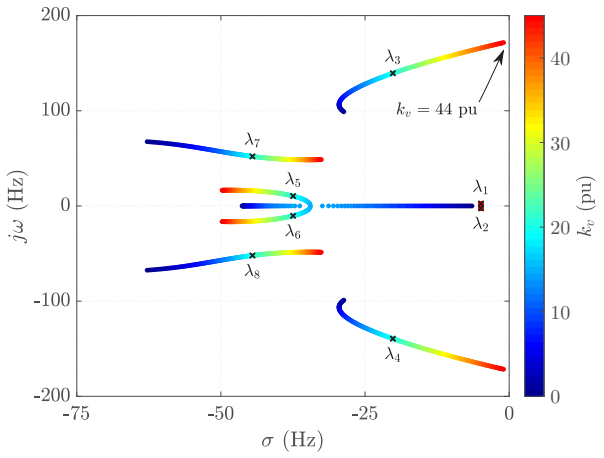

Fig. 7: Eigenvalue trajectory for a sweep of k_v from 1 pu to 44 pu.

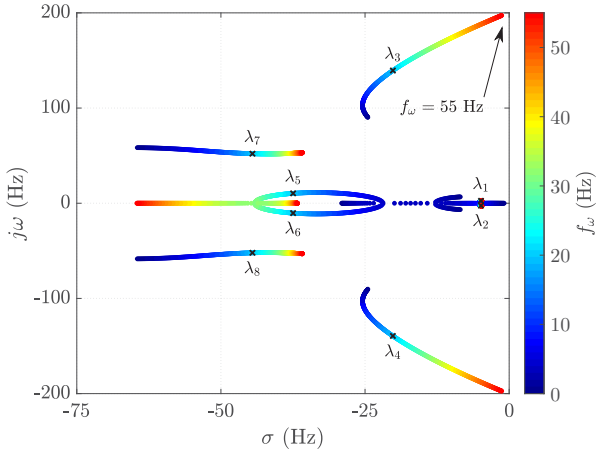

Fig. 8: Eigenvalue trajectory for a sweep of the f_ω from 1 Hz to 55 Hz.

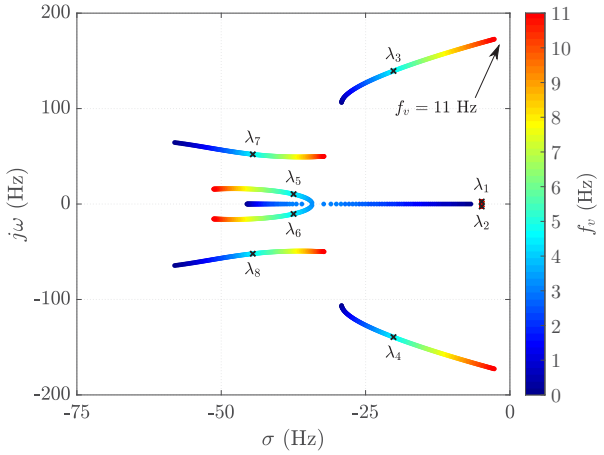

Fig. 9: Eigenvalue trajectory for a sweep of f_v from 1 Hz to 11 Hz.

This work can be of high importance, considering the utilization this control strategy with large expected variations in grid configurations, operating conditions and system parameters.

References

[1] World Energy Council, "Variable Renewables Integration in Electricity Systems: How to Get it Right," *World Energy Perspective Renewable Intergration*, Sep 2016.

[2] T. Kerdphol, F. S. Rahman, and Y. Mitani, "Virtual inertia control application to enhance frequency stability of interconnected power systems with high renewable energy penetration," *Energies*, vol. 11, no. 4, 2018.

[3] S. D'Arco and J. A. Suul, "Virtual synchronous machines classification of implementations and analysis of equivalence to droop controllers for microgrids," in *PowerTech*. Grenoble: IEEE, Jun 2013, pp. 1–7.

[4] J. Rocabert, A. Luna, F. Blaabjerg, and P. RodrÃŋguez, "Control of power converters in ac microgrids," *IEEE Transactions on Power Electronics*, vol. 27, no. 11, pp. 4734–4749, Nov 2012.

[5] D. Wu, F. Tang, J. C. Vasquez, and J. M. Guerrero, "Control and analysis of droop and reverse droop controllers for distributed generations," in *2014 IEEE 11th International Multi-Conference on Systems, Signals Devices (SSD14)*, Feb 2014, pp. 1–5.

[6] V. Mariani, F. Vasca, J. C. VÃąsquez, and J. M. Guerrero, "Model order reductions for stability analysis of islanded microgrids with droop control," *IEEE Transactions on Industrial Electronics*, vol. 62, no. 7, pp. 4344–4354, Jul 2015.

[7] U. B. Tayab, M. A. B. Roslan, L. J. Hwai, and M. Kashif, "A review of droop control techniques for microgrid," *Renewable and Sustainable Energy Reviews*, vol. 76, pp. 717–727, 2017.

[8] N. Bottrell, M. Prodanovic, and T. C. Green, "Dynamic stability of a microgrid with an active load," *IEEE Transactions on Power Electronics*, vol. 28, no. 11, pp. 5107–5119, Nov 2013.

[9] K. D. Brabandere, "Voltage and Frequency Droop Control in Low Voltage Grids by Distributed Generators with Inverter Front-End," Ph.D. dissertation, Katholieke Universiteit Leuven, 2006.

[10] P. Raboni, "Modelling, Control and Integration of Distributed Generators for Enhanced Ancillary Services," Ph.D. dissertation, Aalborg University, 2016.

[11] X. Wang, L. Harnefors, and F. Blaabjerg, "A unified impedance model of grid-connected voltage-source converters," *IEEE Transactions on Power Electronics*, vol. 33, no. 2, pp. 1775–1787, Feb 2018.

[12] R. Teodorescu, M. Liserre, and P. Rodríguez, *Grid Converters for Photovoltaic and Wind Power Systems*. Chichester: John Wiley & Sons, Ltd., 2011.

[13] B. Bahrani, S. Kenzelmann, and A. Rufer, "Multivariable-pi-based *dq* current control of voltage source converters with superior axis decoupling capability," *IEEE Transactions on Industrial Electronics*, vol. 58, no. 7, pp. 3016–3026, Jul 2011.

[14] L. Harnefors, A. G. Yepes, A. Vidal, and J. Doval-Gandoy, "Passivity-based stabilization of resonant current controllers with consideration of time delay," *IEEE Transactions on Power Electronics*, vol. 29, no. 12, pp. 6260–6263, Dec 2014.

[15] D. Pan, X. Ruan, C. Bao, W. Li, and X. Wang, "Capacitor-current-feedback active damping with reduced computation delay for improving robustness of LCL-type grid-connected inverter," *IEEE Transactions on Power Electronics*, vol. 29, no. 7, pp. 3414–3427, Jul 2014.

[16] "*IEEE Guide for Planning DC Links Terminating at AC Locations Having Low Short-Circuit Capacities*," IEEE Std 1204-1997(R2003), pp. 1–216, Jan 1997.

[17] P. Kundur, *Power System Stability and Control*, ser. The EPRI Power System Engineering Series. New York: McGraw-Hill, Inc., 1994.